Chemical Engineering Journal 430 (2022) 131467

Contents lists available at ScienceDirect

Chemical Engineering Journal

journal homepage: www.elsevier.com/locate/cej

A novel strategy for improving SERS activity by cerium ion f → d transitions for rapid detection of endocrine disruptor

Ming Gao [a,b,c,*], Jiacheng Yao [a,b,c,d], Jia Li [a,b,c], Rui Su [e], Yang Liu [a,b,c], Lei Chen [a,b,c], Jinghai Yang [a,b,c]

[a] Key Laboratory of Functional Materials Physics and Chemistry of the Ministry of Education, Jilin Normal University, Changchun 130103, China
[b] National Demonstration Centre for Experimental Physics Education, Jilin Normal University, Siping 136000, China
[c] Key Laboratory of Preparation and Application of Environmental Friendly Materials, Jilin Normal University, Ministry of Education, Changchun 130103, China
[d] Key Laboratory of Artificial Micro- and Nano-structures of Ministry of Education of China, School of Physics and Technology, Wuhan University, Wuhan 430072, China
[e] Changchun Institute of Optics Fine Mechanics and Physics, Chinese Academy of Sciences, Changchun 130103, China

ARTICLE INFO

Keywords:
SERS
$Zn_{1-x}Ce_xO$
Charge transfer
f→d transitions
Trace detection

ABSTRACT

Semiconductor doping offers a wide range of applications in fields from catalysis to electronics. However, for Surface-enhanced Raman spectroscopy (SERS), not many studies are conducted for the commercialisation of this technology. A simple method was developed to synthesise ultra-stable, repeatable, uniform Ce-doped ZnO ($Zn_{1-x}Ce_xO$) with a high SERS activity. The SERS signals of 4-MPy collected on $Zn_{1-x}Ce_xO$ exhibited 118 times higher enhancement than those of ZnO. Cerium ion f → d transitions dominated Charge transfer (CT) is the main cause for this enhancement. The prepared $Zn_{1-x}Ce_xO$ nanoparticles (NPs) can be used to detect Bisphenol A (BPA) with a detection limit of 0.0001 ppm. To our best knowledge, this is the optimum performance reported for semiconductor substrates. Our work paves a way towards highly sensitivity, great-uniformity, high-stability, fast-detection and cost-effective SERS substrates, which can be a promising tool in high-sensitivity contaminant monitoring.

1. Introduction

Exploiting the impurities in semiconductor materials has fundamentally affected in designing their unique electrical, optical and magnetic properties [1–3]. In particular, lanthanide (Ln)-doped semiconductors have attracted enormous attention due to their unique Charge transfer (CT) mechanism. On one hand, their 4f-level electron photoexcitation transition enables the conversion of a low-energy incident laser into high-energy photons [4–6]. On the other hand, their photo-excited states show a high catalytic reduction capacity [7–9]. In light of the aforementioned photoexcited transitions and the reducing power of the excited states, Ln doped semiconductors can serve as promising SERS substrates, which relies on the CT processes between the SERS-active material and the chemisorbed analyte molecules [10–13]. However, few SERS substrate based on Ln-doped semiconductors has been reported.

In the lanthanide series, Ce is highly concentrated due to the excitation and emission of the dipole 4f → 5d, which can provide considerable energy conservation without any loss through the spin-state change [8,14,15]. For semiconductors, ZnO-based nanomaterials are promising due to their rich reserves and high optical stability [16,17]. Ce-doped ZnO temporarily generates charge carriers and facilitates oxygen vacancies formation. Moreover, Ce can lead to decrease in the large band gap of ZnO by forming various optically active sub-levels within the band gap. These characteristics of oxygen vacancies, charge carriers and band gap reduction are conducive to improve the SERS activity; however, these are pursued to a limited extent in the SERS field. Ce-doped ZnO-based SERS may shed light on the poorly explored chemical enhancement mechanism.

Herein, for the first time, we developed Ce-doped ZnO based SERS substrates via a facile chemical precipitation method. As the most abundant lanthanide resource in nature, Ce element is doped into the resourceful ZnO nanomaterials, which provides a facile way towards cost-effective SERS substrates. The synthesized $Zn_{1-x}Ce_xO$ NPs

* Corresponding author at: Key Laboratory of Functional Materials Physics and Chemistry of the Ministry of Education, Jilin Normal University, Changchun 130103, China.
E-mail address: gaomingphy@126.com (M. Gao).

https://doi.org/10.1016/j.cej.2021.131467
Received 27 April 2021; Received in revised form 2 July 2021; Accepted 19 July 2021
Available online 10 August 2021

exhibited excellent SERS activity with an enhancement factor of 7.3 × 10^5, which is more than 3 orders higher than the previously reported semiconductor SERS substrates. Meanwhile, our $Zn_{1-x}Ce_xO$ NPs showed great SERS uniformity and high stability. With 4-mercaptopyridine (4-MPy) molecule as an probe, the CT mechanism of the $Zn_{1-x}Ce_xO$ based SERS substrates is studied. We then applied the $Zn_{1-x}Ce_xO$ based SERS substrates to the trace detection of endocrine disruptor Bisphenol A (BPA), and achieved ultra-sensitive detection (detection limit < 0.0001 ppm) within one minute. Our work sheds light into the Ln enhanced SERS substrates as well as their CT, and provides a facile method towards highly sensitivity, great-uniformity, high-stability, fast-detection and cost-effective SERS substrates, which can be a promising tool in high-sensitivity contaminant monitoring.

2. Experimental

2.1. Synthesis of Ce-doped ZnO nanoparticles

The $Zn_{1-x}Ce_xO$ Nanoparticles (NPs) were prepared by co-precipitation method [18]. First, Zinc nitrate hexahydrate and cerium nitrate hexahydrate were dissolved in deionized water with different molar ratios (the ratio x = Ce/(Ce + Zn) = 0.000, 0.001, 0.005 and 0.010). After stirring for 20 min, the NH_4HCO_3 aqueous solution was added. Then, the mixture was stirred for 4 h before being washed by centrifugation. Finally, the mixture was dried under vacuum for 12 h, and further annealed in air at 600 °C for 1 h to obtain the final $Zn_{1-x}Ce_xO$ NPs.

2.2. Characterization of Ce-doped ZnO nanoparticles

Then, the structure of the as-prepared samples was investigated with X-ray diffraction (XRD, Rigaku D/Max 3C). X-ray photoelectron spectra (XPS, VG ESCALAB 250X) and coupled plasma atomic emission spectroscopy (ICP-AES, Perkin-Elmer 7000 DV) were implemented to analyze the element concentration. JEM-2100HR transmission electron microscope (TEM) was used to characterize the morphology. The UV–vis absorption spectra were measured by Shimadzu 3600 spectrometer. All SERS measurements were carried out with a Renishaw inVia Raman instrument. The excitation source is a 514.5 nm Ar^+ ion laser (2.41 eV) with a laser power of 40 mW (attenuation: 10%; exposure time: 10 s; 1 scan). For the mapping experiments, an automapping stage with an approximate 5 × 5 μm^2 area was chosen to investigate the distribution of the SERS signal by using the static measurement model (the acquisition time was 1 s, accumulation was 1 time, and the scanning step was 1 μm).

2.3. The SERS experiments of BPA

To investigate the SERS sensitivity of $Zn_{1-x}Ce_xO$, we adopted BPA solution as the trace analytes. First, the Pauly's reagents (reagent A: p-aminobenzene sulfonic acid and 5 ml 12 M HCl solution; reagent B: 5% $NaNO_2$; reagent C: Na_2CO_3) were mixed in a volume ratio of 1:1:1 and stored at 4 °C. The mixed Pauly's reagents served as a coupling agent, which can increase the adhesion of BPA to the $Zn_{1-x}Ce_xO$ surface. Second, the as-prepared $Zn_{1-x}Ce_xO$ NPs were dissolved in deionized water to form a solution, and were then mixed with the coupling agent and the analyte BPA in a volume ratio of 2:1:1. Thrid, the obtained mixture was poured into an aluminum pan for testing. Here, the excitation source is a 514.5 nm laser with a laser power of 80 mW (attenuation: 50%; exposure time: 30 s; spectral range: 900–1800 cm^{-1}; 1 scan per spectrum). The whole trace detection process was completed in one minute. We analyzed the data by WiRE that comes with the software of the Raman instrument. We use WiRE software to eliminate the cosmic ray and fluorescence background of all SERS spectra, and then use Origin software for data sorting and comparison.

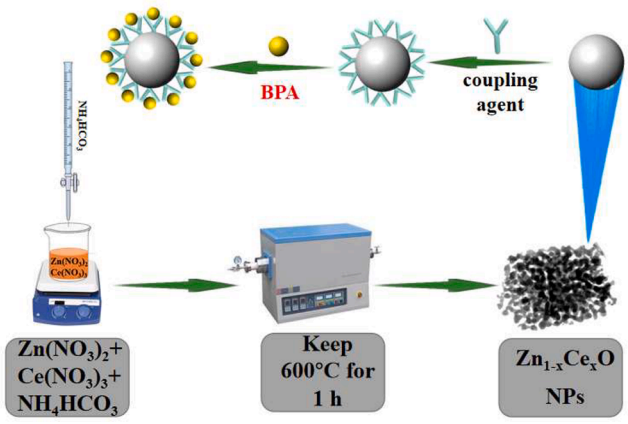

Fig. 1. The preparation scheme of $Zn_{1-x}Ce_xO$ NPs and the rapid detection process of BPA.

3. Results and discussion

Fig. 1 shows the preparation scheme of $Zn_{1-x}Ce_xO$ NPs and the rapid detection process of BPA. The whole trace detection process can be completed within one minute. To evaluate the effect of Ce doped concentration on the SERS activity of ZnO, we applied 4-MPy as an probe. According to Ref. 19, the SERS spectra of 4-MPy adsorbed ZnO NPs are almost identical to those of pure ZnO NPs [19]. With the existence of 4-MPy, the SERS spectra of $Zn_{1-x}Ce_xO$ are shown in Fig. 2a. A complete assignment of the most intense bands is presented in Fig. 2b. To clearly observe the change of spectral intensity, the SERS intensity of the 1593 cm^{-1} band of 4-MPy is plotted as a function of the Ce concentration, as shown in Fig. 2c. As it can be clearly seen, the peak intensity increases with the Ce doping concentration (x) before reaching the maximum (x = 0.5%), and drops down when x goes up to 1%. It's worth mentioning that, all 4-MPy molecules on $Zn_{1-x}Ce_xO$ substrates exhibit ultra-high SERS enhancement. Even with only 0.1% doping concentration, the SERS enhancement of the $Zn_{1-x}Ce_xO$ substrates is 70 times stronger than that of pure ZnO, and the SERS intensity of $Zn_{0.995}Ce_{0.005}O$ substrates is as high as 118 times stronger than that of pure ZnO substrates. This may attribute to the semiconductor's molecular CT mechanism because Surface plasmon resonance (SPR) is far from laser excitation wavelength [20]. To have a quantitative evaluation on the contribution of CT in the SERS mechanism, we further investigated into the ratio of the asymmetric vibration mode to the fully symmetric vibration mode.

According to the method proposed by Lombardi et al., the relative CT contribution for each mode can be given as: [21]

$$\rho_{CT}(k) = \frac{I^k(CT) - I^k(SPR)}{I^k(CT) + I^o(SPR)} \quad (1)$$

where k is an indicator of a single molecular line in the Raman spectrum. Here, we chose the vibration peak intensities – 1118 cm^{-1} (totally symmetric a_1 vibrations modes) and 1593 cm^{-1} (non-totally symmetric b_2 vibrations modes) - as two reference lines. $I^0(SPR)$ is the intensity of the 1118 cm^{-1} peak (a_1) with the SERS signals contributed by SPR, and $I^k(CT)$ is the intensity of the 1593 cm^{-1} peak (b_2). $I^k(CT)$ is the measured intensity of the line (k) where CT resonance has an additional contribution to the SERS intensity. Note that for totally symmetric line, $I^k(SPR) = I^0(SPR)$, and for non-totally symmetric line, $I^k(SPR)$ is usually small or zero. ρ_{CT} ranges from 0 to 1, and the larger ρ_{CT} is, the more dominant the CT contribution is. From Eq. (1), we calculated the ρ_{CT} and plotted its trend as a function of the Ce doping concentration. As shown in Fig. 2d, ρ_{CT} first increased with the Ce doping concentration and reached its maximum when the Ce concentration was 0.5%. Then ρ_{CT} droped down when the Ce concentration rose up to 1%. So it's safe to say, the CT contribution of ZnO is greatly increased after doping Ce, but

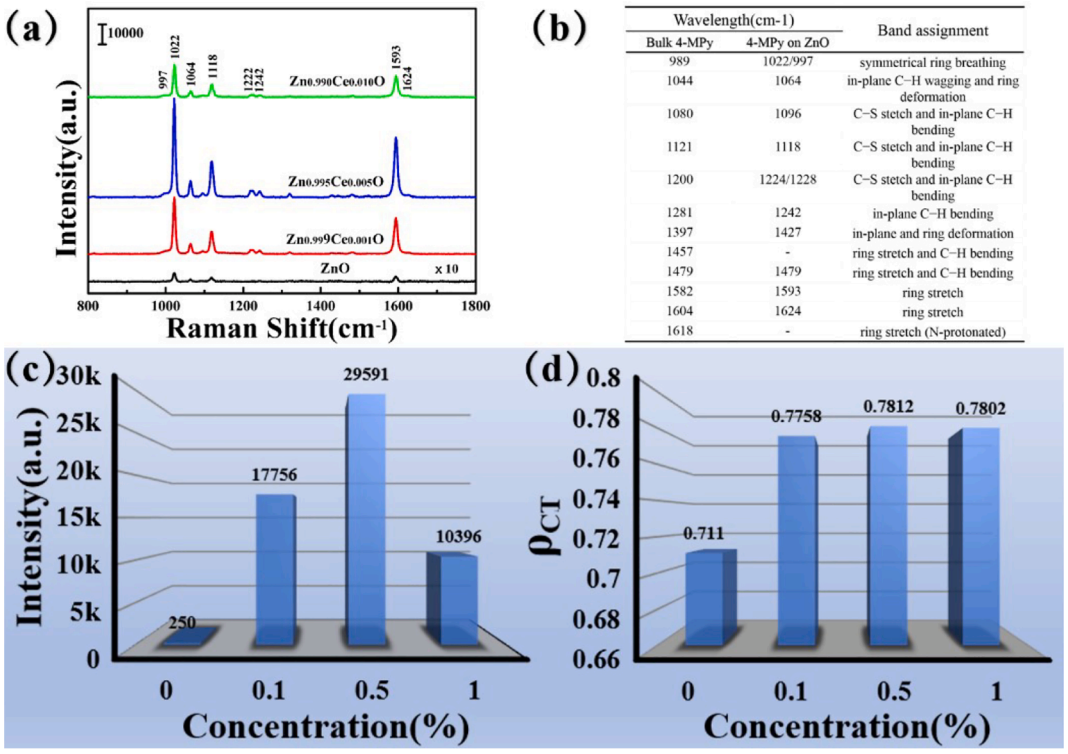

(b)

Wavelength(cm-1)		Band assignment
Bulk 4-MPy	4-MPy on ZnO	
989	1022/997	symmetrical ring breathing
1044	1064	in-plane C−H wagging and ring deformation
1080	1096	C−S stetch and in-plane C−H bending
1121	1118	C−S stetch and in-plane C−H bending
1200	1224/1228	C−S stetch and in-plane C−H bending
1281	1242	in-plane C−H bending
1397	1427	in-plane and ring deformation
1457	-	ring stretch and C−H bending
1479	1479	ring stretch and C−H bending
1582	1593	ring stretch
1604	1624	ring stretch
1618	-	ring stretch (N-protonated)

Fig. 2. (a) SERS spectra of 4-MPy adsorbed on ZnO and $Zn_{1-x}Ce_xO$; (b) Corresponding assignment of the most intense bands; (c) A plot of the SERS intensity of the 1593 cm^{-1} band of 4-MPy versus Ce concentration. (d) A plot of the ρ_{CT} versus Ce concentration.

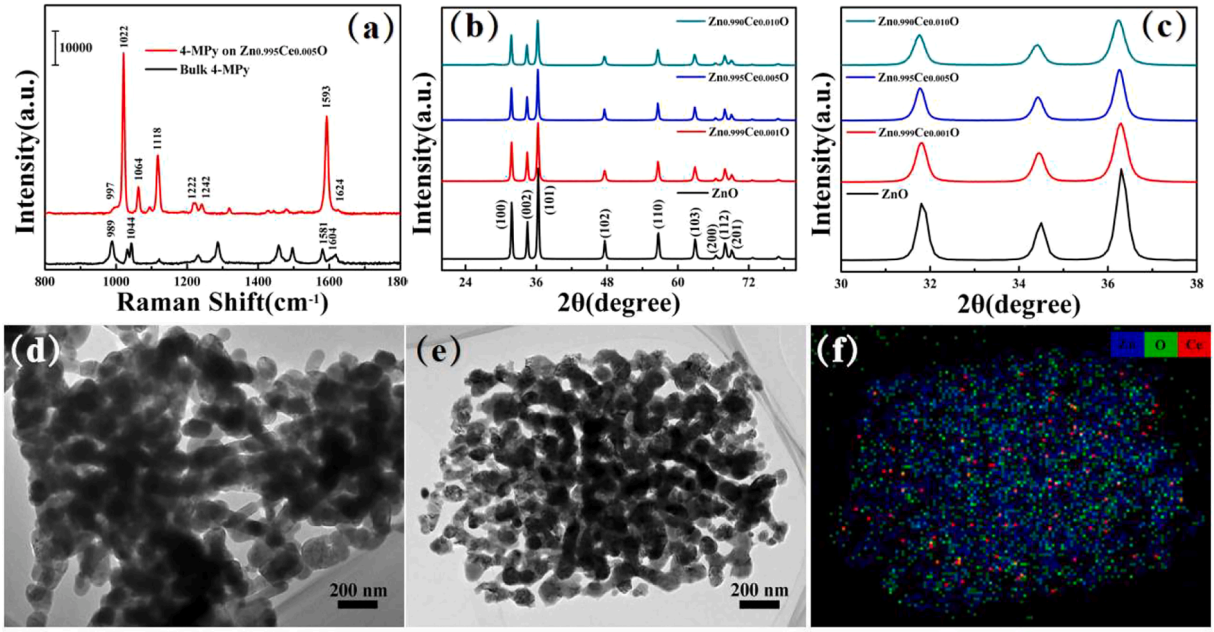

Fig. 3. (a) Comparison of the Raman spectrum of bulk 4-MPy and the SERS spectrum of 4-MPy on $Zn_{0.995}Ce_{0.005}O$; (b) The XRD patterns of the ZnO and $Zn_{1-x}Ce_xO$; (c) An enlarged version of the XRD spectra when 2θ ranges from 30° to 38°; (d) TEM image of ZnO; (d) TEM image of $Zn_{0.995}Ce_{0.005}O$; (f) Element mapping of $Zn_{0.995}Ce_{0.005}O$.

the relationship of doping concentration versus CT contribution is not obvious.

Further, we made a rough estimation of the Enhancement factor (EF) of $Zn_{0.995}Ce_{0.005}O$ substrates via: [22]

$$EF = \frac{I_{SERS}N_{Bulk}}{I_{Bulk}N_{SERS}} = \frac{I_{SERS}}{I_{Bulk}} \times \frac{S_{laser} \times h \times C \times N_A}{S_{laser}/S_{MPy}} \quad (2)$$

where I_{SERS} and I_{Bulk} are the spectrum intensities of the 4-MPy on the $Zn_{0.995}Ce_{0.005}O$ substrates and the bulk 4-MPy, respectively (Fig. 3a, at 1593 cm^{-1}). Hence, we can obtain that I_{SERS}/I_{Bulk} = 29591/4683 = 6.32. Moreover, S_{laser} is laser spot size of 1 μm. C is the corresponding concentration of 4-Mpy used in the Raman spectra of 10.8 M (using the density 1.2 g/cm^3 and molar mass 111.16 g/mol), h is the effective layer

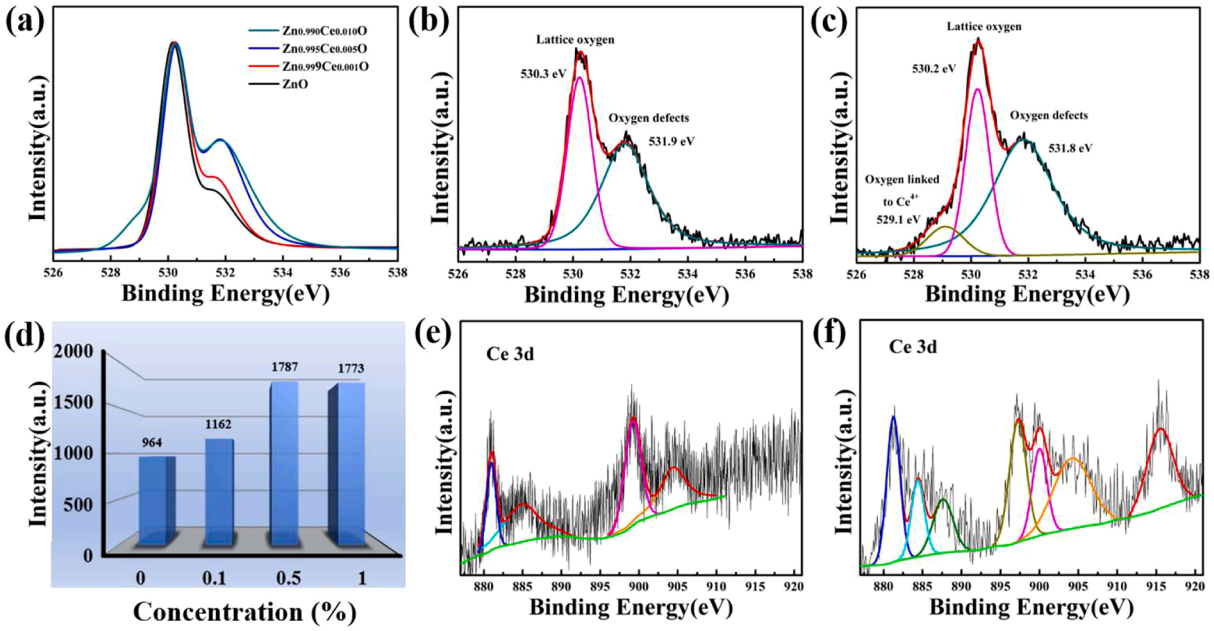

Fig. 4. (a) O 1s XPS spectra for ZnO and $Zn_{1-x}Ce_xO$; (b) O 1s XPS spectra for $Zn_{0.995}Ce_{0.005}O$; (c) O 1s XPS spectra for $Zn_{0.99}Ce_{0.01}O$; (d) A plot of the XPS intensity of the 531.9 eV in O1s region versus Ce concentration; (e) Ce 3d XPS spectra for $Zn_{0.995}Ce_{0.005}O$; (f) Ce 3d XPS spectra for $Zn_{0.995}Ce_{0.01}O$.

depth of 19 μm. NA is the Avogadro constant. S_{MPy} is the area of each 4-Mpy molecule ($\sim 7 \times 10^{-7}$ μm^2) [23]. By dividing the laser surface area by the cross-sectional area per molecule. Thus, we can then obtain N_{SERS} is 9.70×10^{10} and N_{Bulk} is 1.12×10^6, the resulting EF is $\sim 7.3 \times 10^5$, which is more than 3 orders higher than that of the previously reported semiconductor nanomaterials [24,25].

Fig. 3b shows the XRD patterns of the pure ZnO and the $Zn_{1-x}Ce_xO$ substrates. All diffraction peaks are consistent with the wurtzite hexagonal phase of ZnO (JCPDS card no. 36-1451). Moreover, weak signals corresponding to the (111) diffraction plane of cubic CeO_2 can be observed at $2\theta = 28.6°$ (JCPDS No 34-0394) for the highest doping (x = 1), which indicated that the Ce ions precipitated in the form of CeO_2 due to saturation and did not disrupt the ZnO crystal structure [26]. At low Ce doping concentration, no peaks for Ce-related compound could be identified, indicating that Ce^{3+} ions are uniformly substituted into the interstitial sites in ZnO lattice. An enlarged version of the XRD spectra between 30° and 38° is shown in Fig. 3c, from which we can see that the (100), (002) and (101) peaks have shifted a little due to the mismatch of ionic radii, demonstrating that the doped Ce is at least partly incorporated into the ZnO lattice. This is consistent with the previous report that the Ce^{3+} ions can lead to the gradual decrease of the average crystallite size, and make the NPs more densely packed [27]. Fig. 3d–e shows the TEM images of pure ZnO and $Zn_{0.995}Ce_{0.005}O$ substrates. All ZnO and $Zn_{0.995}Ce_{0.005}O$ NPs are quasi-spherical and dispersed homogeneously. The pure ZnO NPs (Fig. 3d) are a random cluster of nanoparticles, while the $Zn_{0.995}Ce_{0.005}O$ NPs (Fig. 3e) aggregate into sheets. The grain size and density of NPs decrease after the Ce doping, which is consistent with the XRD results. Chemical composition was further confirmed through the element mapping, as shown in Fig. 3f.

To find out how the dopants in semiconductors affect the SERS enhancement mechanism, we further investigated into the XPS spectra of $Zn_{1-x}Ce_xO$ substrates. Fig. 4a is the normalized XPS spectrum at 530.3 eV. As it can be seen in Fig. 4a, the peak position of the lattice oxygen is changed with the doping concentration, which is because the binding energy of Ce^{3+}/Ce^{4+} ion and Zn^{2+} ion to O^{2-} ion is different. As shown in Fig. 4d, the oxygen-deficient peak first increases with the Ce concentrations until reaching the maximum when the doping concentration is 0.5%, the peak decreases when the concentration rises up to 1%. Fig. 4b shows the O 1 s signal of $Zn_{0.995}Ce_{0.005}O$. Through Lorentzian Gaussian, the O 1 s signal can be fitted into two peaks located at 530.3 eV and 531.9 eV, which are attributed to the O^{2-} ions in the metal oxide (lattice oxygen) and the oxygen-deficient regions, respectively.[28] In comparison, Fig. 4c shows the O 1 s signal of $Zn_{0.990}Ce_{0.010}O$ which can be fitted into three peaks. The peak located at 529.1 eV can be assigned to the oxygen linked to Ce^{4+}, which further proves the precipitation of CeO_2 [29]. This also explains the decrease of the oxygen-deficient peak at the maximum Ce doping. Fig. 4e shows the Ce (3d) XPS spectrum of $Zn_{0.995}Ce_{0.005}O$, which could be spitted into four peaks. The characteristic peak at 881.25 eV, 884.39 eV, 900.01 eV and 904.34 eV indicates the existence of Ce^{3+} in $Zn_{0.995}Ce_{0.005}O$ [30]. The peaks at 915.56 eV indicate the transition of Ce^{4+} between energy levels [31,32] In contrast, the Ce 3d XPS spectrum of $Zn_{0.990}Ce_{0.010}O$ shows two additional peaks. Peaks at 887.68 eV and 897.30 eV are attributed to Ce $3d_{5/2}$ photoemission lines of CeO_2.[33,34] The practical doping concentration and the elemental analysis of the samples were investigated by ICP-AES (Table S1), which showed that the practical Ce concentrations are a little larger than the theoretical ones. This may be due to unreacted Zn ions being washed away.

As shown in Figs. 4d and 2d, the change in the oxygen defects is not completely consistent with the change in the ρ_{CT}. As we all know, most lanthanide ions undergo the electronic transition of 4f → 4f when excited. Since the electrons in the 4f orbital are effectively shielded by the 5s and 5p electrons in the outer layer, the 4f energy level structure basically retains the free ion property. However, the Ce^{3+} ion has only one 4f electron, which will be transited to the 5d level after excitation, and no shielding of the outer electrons exists. Therefore, the excited state of Ce^{3+} ion can easily lose its sole electron in the 5d orbit and become a tetravalent Ce ion. If the Ce^{4+} ion captures an electron, it changes back to the trivalent Ce ion [7,8]. The relative reactions can be showed as follows:

$$Ce^{4+} + e^- \rightarrow Ce^{3+} \quad (3)$$

So a quick $Ce^{4+} \leftrightarrow Ce^{3+}$ reaction can increase the fast electron transfer and enhance the SERS intensity. It indicates that the oxygen deficiency is only one of the enhancement factors, the main reason should be related to the doped Ce^{3+} ions.

Then, we studied the effect of Ce doping on the band gap of ZnO, UV–VIS reflectance absorption spectra (Fig. S1) indicates the $Zn_{1-x}Ce_xO$

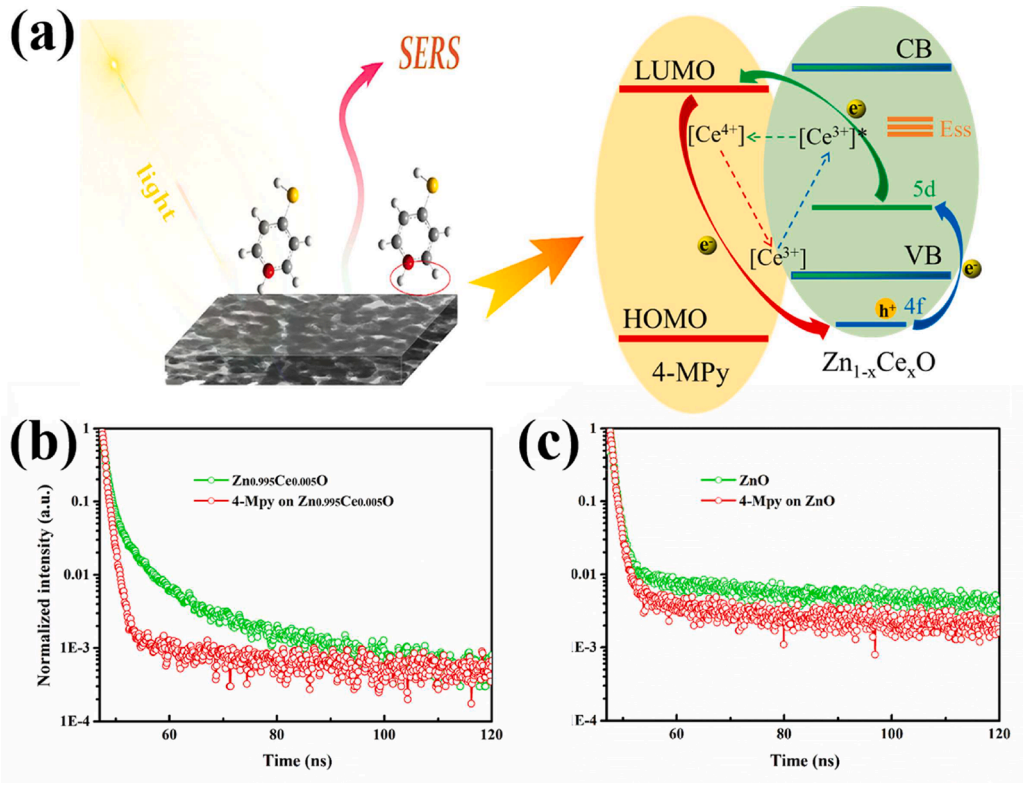

Fig. 5. (a) The proposed charge-transfer mechanism between 4-MPy and $Zn_{0.995}Ce_{0.005}O$; Evolution of lifetime decays for (b) $Zn_{0.995}Ce_{0.005}O$ and (c) ZnO before and after adsorbing 4-MPy molecules at the green emission bands. (For interpretation of the references to color in this figure legend, the reader is referred to the web version of this article.)

has more excellent surface properties (plentiful surface defects) than pure ZnO, and the interband charge transition in Ce doped ZnO samples are easier and thus have more preferable optical absorption properties (more details can be seen in Supporting information).

Based on the foregoing discussions, the CT mechanism of $Zn_{1-x}Ce_xO$ is illustrated in Fig. 5. First, more surface oxygen vacancy defects will be created after doping. The defects can capture electrons and form the surface state energy levels (Ess), which inhibits the recombination of photon-generated carriers (electrons and holes) in ZnO and promotes the CT between the substrate and the probe molecule. Then, Ce^{3+} ions

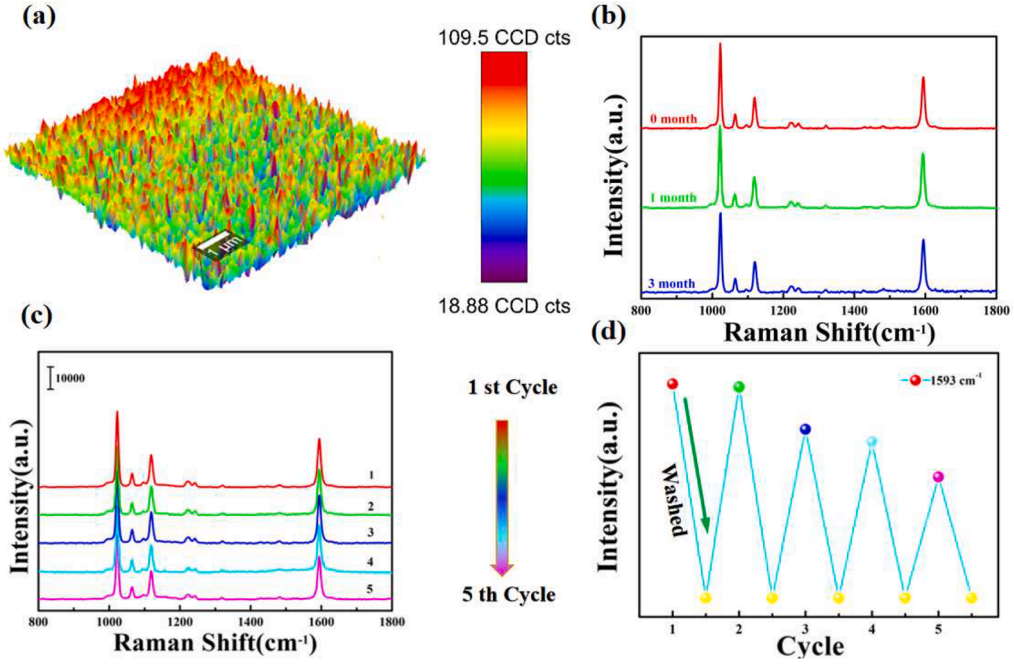

Fig. 6. (a) The SERS mapping 3D-image in the intensity distribution of the 4-MPy Raman peak at 1593 cm^{-1}; (b) SERS spectra of 4-MPy on $Zn_{0.995}Ce_{0.005}O$ collected at different time; (c) SERS spectra for reusability test, then washed for five continuous cycles; (d) variation of 1593 cm^{-1} integral peak intensity with washing cycle.

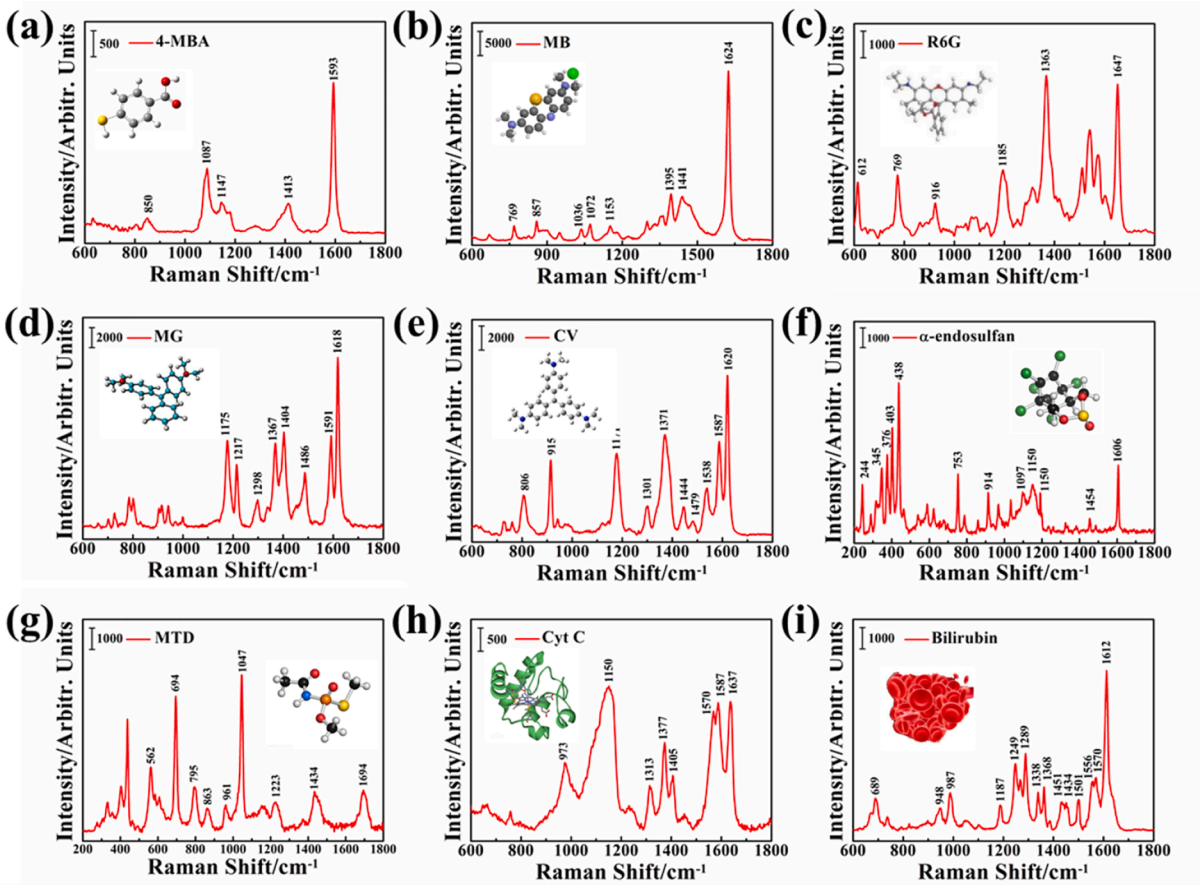

Fig 7. SERS spectram of (a) 4-MBA; (b) MB; (c) R6G; (d) MG, (e) CV; (f) α-endosulfan; (g)MTD; (h) Cyt C; (i) Bilirubin based on $Zn_{0.995}Ce_{0.005}O$.

are excited to conduct 4f → 5d electronic transition ($[Ce^{3+}] \rightarrow [Ce^{3+}]^*$). The electrons of the excited 5d orbital can directly jump to the lowest unoccupied molecular orbital (LUMO) of the probe molecule or transited to Ess ($[Ce^{3+}]^* \rightarrow [Ce^{4+}]$). Finally, the electrons are transferred back to the ground state of Ce ions after releasing Raman photons ($[Ce^{4+}] \rightarrow [Ce^{3+}]$).

This additional charge transfer mechanism caused by Ce ions is a good explanation for the significant increase in CT contributions (ρ_{CT}) after doping Ce. The incorporation of Ce caused a qualitative change, which brings a huge change in CT contributions (ρ_{CT}). In comparison, the change in doping concentration is only a quantitative change, thus resulting in a relatively small change in CT contributions (ρ_{CT}). Moreover, the 5d energy level of the excited state is above the Valence band (VB) of ZnO. As the Ce doping concentration increases, the oxygen deficiency increases, and the optical band gap becomes narrower, making CT easier and resulting in the increase in SERS peak intensity. When the doping concentration increases to a certain degree, CeO_2 is precipitated and the presence of Ce^{4+} will inhibit the conversion of the Ce ions valence state, which reduces the SERS activity. This can explain why the SERS activity of $Zn_{0.99}Ce_{0.01}O$ substrates is weaker than that of $Zn_{0.995}Ce_{0.005}O$ substrates. Furthermore, we measured the fluorescence lifetime of $Zn_{0.995}Ce_{0.005}O$ before and after adsorbing 4-MPy molecules, as shown in Fig. 5b. It was found that the fluorescence lifetime decreased rapidly after adsorbing 4-MPy molecules, owing to the fluorescence quenching caused by the electron transfer of Ce ions. It's worth noting that, the fluorescence lifetime of ZnO before and after adsorbing 4-MPy molecules is almost unchanged in Fig. 5c. Therefore, Ce ions are considered as the main reason for SERS enhancement.

A commercial SERS substrate should not only have high SERS activity but also show good homogeneity (distribution uniformity), stability and reusability. To characterize the SERS enhancement distribution on the $Zn_{0.995}Ce_{0.005}O$ NPs, the SERS mapping 3D-image which exhibits the intensity distribution of the 4-MPy Raman peak (at 1593 cm^{-1}) is measured by a color decoding method, as shown in Fig. 6a. Meanwhile, the measured Raman spectra are shown in Fig. S2, indicating that the peak position and the peak intensity of all spectra are almost the same. The Relative standard deviation (RSD) for the peak at 1593 cm^{-1} was calculated at 6.27%, which points to great repeatability of the $Zn_{0.995}Ce_{0.005}O$ NPs as a SERS substrate. In practical applications, the stability of SERS substrates is another crucial issue that must be considered. Fig. 6b shows the SERS spectrum of 4-MPy on $Zn_{0.995}Ce_{0.005}O$ with time, results showed that the peak intensity of 4-MPy was almost constant with time, indicating that the $Zn_{0.995}Ce_{0.005}O$ substrate has extremely high stability. Table S2 listed the storage time of three recently reported substrates compared with our proposed $Zn_{0.995}Ce_{0.005}O$ substrate, and our substrate shows 90 days which is the longest stability than the previous substrates. Another main concern is that a reusable SERS substrate will not only reduce cost for practical applications, but also supports sustainability as an environmentally friendly solution. To test the reusability of the $Zn_{0.995}Ce_{0.005}O$, 4-MPy (10^{-3} M) was added and the corresponding SERS spectrum was obtained, and then, thoroughly washed with ethanol and deionized water until the spectrum intensity disappeared. Repeat this process of 4-MPy (10^{-3} M) was added and washed for five consecutive cycles as shown in the Fig. 6c. The corresponding intensity values of 1593 cm^{-1} was plotted in Fig. 6d, showing that the $Zn_{0.995}Ce_{0.005}O$ has excellent recyclability capacity for the practical applications. Universality is one of the ultimate goals of SERS substrate development. Fig. 7 shows the Raman signals of common molecules [4-mercaptobenzoic acid (4-MBA)], fungicides [thiram, Malachite green (MG), Methylene blue (MB), Crystal violet (CV)], pesticides [α-endosulfan, Methamidophos (MTD)] and biological molecules [Cytochrome *C* (Cyt C), Bilirubin] by

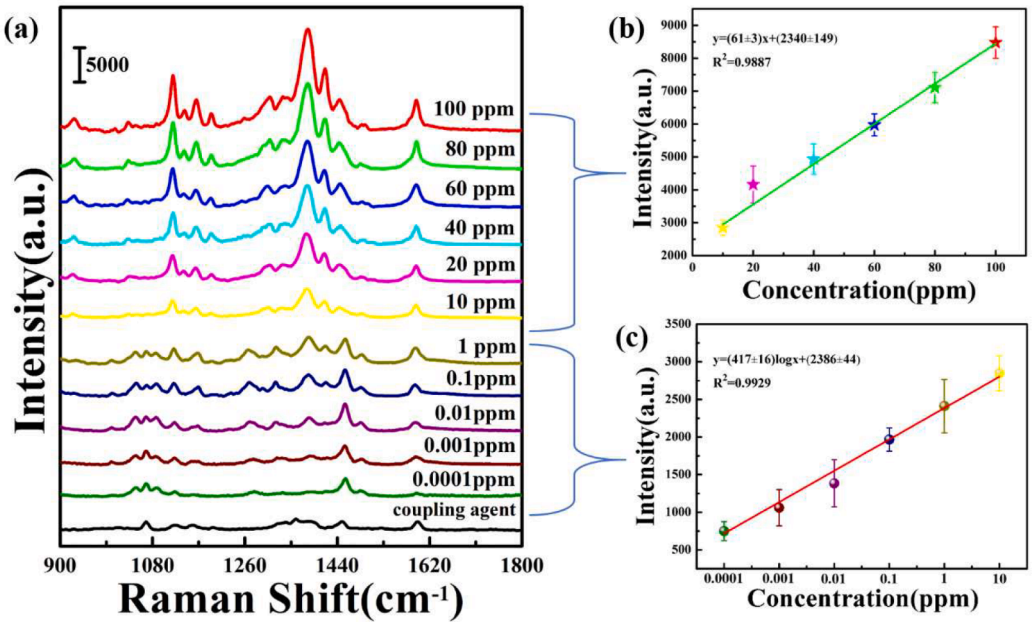

Fig. 8. (a) SERS spectra of BPA with concentrations ranging from 0.0001 to 100 ppm, with the existence of $Zn_{0.995}Ce_{0.005}O$ and coupling agent; The peak intensity of SERS spectra at 1121 cm $^{-1}$ as a function of BPA concentrations ranging from: (b) 10 to 100 ppm (c) 0.0001 to 10 ppm.

Table 1
Detection limits of BPA on semiconductor based SERS substrates.

SERS substrates	LOD	Ref
MoO_2 nanodumbbells	10^{-7} M	Zhang et al. [42] 2018
monolayer graphene-coated Ag nanoparticles	1 μg/L (4×10^{-9} M)	Qiu et al. [43] 2018
Self- assembled Graphitic	10^{-6} M	Pei et al. [44] 2017
GO/Ag/TiO_2 NT	5×10^{-7} M	Xie et al. [45] 2014
$Zn_{0.995}Ce_{0.005}O$	0.0001 ppm (4×10^{-10} M)	This work

using $Zn_{0.995}Ce_{0.005}O$ as the SERS substrate, which demonstrates the capability of our proposed $Zn_{0.995}Ce_{0.005}O$ substrates as ultrasensitive sensing tools in broad fields. All spectra of these different molecules are consistent with the previously reports [13,28,35–38].

Our proposed SERS substrate was then applied to the trace detection of endocrine disruptor BPA, a notorious contaminant in the environment and the food chain which can harm humans at even 2.5 ppm [39,40]. Compared with various traditional methods of detecting BPA, we found that our method takes the shortest time (Table S3). The whole detection process was completed within 1 min.

The SERS spectra of pure coupling agent and different concentrations of BPA (100–0.0001 ppm) are shown in Fig. 8a, there are several significant spikes, which are generally consistent with the previously reports [41]. The peak intensity gradually decreases with the decrease of BPA concentration but is still visible when the BPA concentration is 0.0001 ppm, which means the detection limit can reach 0.0001 ppm. As seen inFig. 8b and 8c, the normalized Raman signal intensity at 1118 cm^{-1} is linearly related to the BPA concentrations in the range of 100–10 ppm and 1–0.0001 ppm, respectively (more details can be seen in Supporting information). But a significant drop happens when the BPA concentration equals 10 ppm. This is because the high concentration of BPA can suppress the SERS response of the coupling agent, so the Raman peak of the coupling agent only appears at low concentrations (<1ppm).

As seen in Table1, four recently reported semiconductor based substrates for detecting BPA is compared with our proposed $Zn_{0.995}Ce_{0.005}O$ substrate, and our method shows more than 1–4 orders higher performance than the previous substrates.

4. Conclusions

In summary, for the first time, we developed Ce-doped ZnO based SERS substrates via a facile chemical precipitation method. Our synthesized $Zn_{0.995}Ce_{0.005}O$ substrate exhibited excellent SERS activity with an enhancement factor of 7.3×10^5, which is more than 3 orders higher than the previously reported semiconductor SERS substrates. The mechanism of the $Zn_{1-x}Ce_xO$ based SERS substrates is proposed, the unique 4f to 5d electron transition is the main reason for SERS enhanceme. When detecting BPA, our proposed substrates can achieve ultrasensitive detection (detection limit < 0.0001 ppm) within one minute. Our work sheds light into the Ln enhanced SERS substrates and provides a facile method towards highly sensitive, great-uniformity, high-stability, fast-detection and cost-effective SERS substrates, which can be a promising tool in high-sensitivity contaminant monitoring.

Declaration of Competing Interest

The authors declare that they have no known competing financial interests or personal relationships that could have appeared to influence the work reported in this paper.

Acknowledgements

This work is supported by the National Natural Science Foundation of China (No. 21776110, 61675090, 61705020 and 21676115); National Youth Foundation of China (No. 51608226, 61705078, and 61704065); Program for the Development of Science and Technology Jilin province (No. 20200301043RQ and 20190103002JH); the Thirteenth Five-Year Program for Science and Technology of Education Department of Jilin Province (JJKH20200418KJ).

Appendix A. Supplementary data

Supplementary data to this article can be found online at https://doi.

org/10.1016/j.cej.2021.131467.

References

[1] T. Senden, R.J.A. van Dijk-Moes, A. Meijerink, Quenching of the red Mn^{4+} luminescence in Mn^{4+}-doped fluoride LED phosphors, Light: Sci. Appl. 7 (2018) 8–20.

[2] Z.W. Jia, C.X. Yuan, Y.F. Liu, X.J. Wang, P. Sun, L. Wang, H.C. Jiang, J. Jiang, Strategies to approach high performance in cr^{3+}-doped phosphors for high-power NIR-LED light sources, Light: Sci. Appl. 9 (2020) 86–94.

[3] N.H. Le, G.V. Lanskii, G. Aeppli, B.N. Murdin, Giant Non-Linear susceptibility of hydrogenic donors in silicon and germanium, Light Sci. Appl. 8 (2019) 64–70.

[4] T.T. Xuan, R.J. Xie, Recent processes on light-emitting lead-free metal halide perovskites, Chem. Eng. J. 393 (2019), 124757.

[5] A. Singh, A. Pashkin, S. Winnerl, M. Welsch, C. Beckh, P. Sulzer, L. Leitenstorfer, M. Helm, H. Schneider, Up to 70 THz bandwidth from an implanted Ge photoconductive antenna excited by a femtosecond Er: fibre laser, Light Sci. Appl. 9 (2020) 30–36.

[6] J. Liu, N.K. Ma, W. Wu, Q.G. He, Recent progress on photocatalytic heterostructures with full solar spectral responses, Chem. Eng. J. 393 (2020), 124719.

[7] Y. Qiao, E.J. Schelter, Lanthanide Photocatalysis, Acc. Chem. Res. 51 (2018) 2926–2936.

[8] G.M. Li, B. Wang, J. Zhang, R. Wang, H.L. Liu, Er-doped g-C_3N_4 for photodegradation of tetracycline and tylosin: high photocatalytic activity and low leaching toxicity, Chem. Eng. J. 391 (2020), 123500.

[9] J.X. Wang, Y. Zhuo, Y. Zhou, H.J. Wang, R. Yuan, Y.Q. Chai, Ceria Doped Zinc Oxide Nanoflowers Enhanced Luminol-Based Electrochemiluminescence Immunosensor for Amyloid-β Detection, ACS Appl. Mater. Interfaces 8 (2016) 12968–12975.

[10] S. Schlücker, Surface-Enhanced raman spectroscopy: concepts and chemical applications, Angew. Chem. Int. Ed. 53 (2014) 4756–4795.

[11] R. Balaji, V. Renganathan, S.M. Chen, V. Singh, Ingenious design and development of recyclable 2D BiOCl nanotiles attached tri-functional robust strips for high performance selective electrochemical sensing, SERS and heterogenous dip catalysis, Chem. Eng. J. 385 (2020), 123974.

[12] X.Y. Zhang, D. Han, N. Ma, R. Gao, A. Zhu, S. Guo, Y. Zhang, Y. Wang, J. Yang, L. Chen, Carrier density-dependent localized surface plasmon resonance and charge transfer observed by controllable semiconductor content, J. Phys. Chem. Lett. 9 (2018) 6047–6051.

[13] J. Yao, Y. Quan, R. Gao, J. Li, L. Chen, Y. Liu, J. Lang, H. Shen, Y. Wang, J. Yang, M. Gao, Improved charge transfer and hot spots by doping and modulating the semiconductor structure: A high sensitivity and renewability surface-enhanced raman spectroscopy substrate, Langmuir 35 (27) (2019) 8921–8926.

[14] X. Qin, X.W. Liu, W. Huang, M. Bettinelli, X.G. Liu, Lanthanide-activated phosphors based on 4f–5d optical transitions: theoretical and experimental aspects, Chem. Rev. 117 (2017) 4488–4527.

[15] H. Yin, P.J. Carroll, J.M. Anna, E.J. Schelter, Luminescent Ce(III) complexes as stoichiometric and catalytic photo-reductants for halogen atom abstraction reactions, J. Am. Chem. Soc. 137 (2015) 9234–9237.

[16] M. Gao, G.Z. Xing, J.H. Yang, L.L. Yang, Y.J. Zhang, H.L. Liu, H.G. Fan, Y.G. Sui, B. Feng, Y.F. Sun, Z.Q. Zhang, S.S. Liu, S. Li, H. Song, Zinc oxide nanotubes decorated with silver nanoparticles as an ultrasensitive substrate for surface-enhanced raman scattering, Microchim. Acta 179 (2012) 315–321.

[17] G. Sinha, L.E. Depero, I. Alessandri, Recyclable SERS substrates based on Au-Coated ZnO nanorods, ACS Appl. Mater. Interfaces 3 (2011) 2557–2563.

[18] S. Yang, J.C. Yao, Y.N. Quan, M.Y. Hu, R. Su, M. Gao, D.L. Han, J.H. Yang, Monitoring the charge transfer process in a Nd-doped semiconductor based on photoluminescence and SERS technology, Light-Sci. Appl. 9 (2020) 117.

[19] H.Y. Shin, E.L. Shim, Y.J. Choi, J.H. Park, S. Yoon, Giant enhancement of raman response due to one-Dimensional ZnO nanostructures, Nanoscale 6 (2014) 14622–14626.

[20] G. Song, W.B. Gong, S. Cong, Z.G. Zhao, Ultrathin Two-dimensional nanostructures: Surface defects for morphology-driven enhanced semiconductor SERS, Angew. Chem. Int. Ed. Engl. 60 (2020) 5505–5511.

[21] J.R. Lombardi, R.L. Birke, A unified approach to surface-enhanced raman spectroscopy, J. Phys. Chem. C 112 (2008) 5605–5617.

[22] Y.N. Quan, R. Su, S. Yang, L. Chen, M.B. Wei, H.L. Liu, J.H. Yang, M. Gao, B.Z. Li, In-situ surface-enhanced Raman scattering based on MTi_{20} nanoflowers: monitoring and degradation of contaminants, J. Hazard. Mater. 412 (2021), 125209.

[23] X.Q. Fu, F.L. Bei, X. Wang, X.J. Yang, L.D. Lu, Surface-enhanced raman scattering of 4-Mercaptopyridine on Sub-monolayers of α-Fe_2O_3 nanocrystals (Sphere, Spindle, Cube), J. Raman Spectrosc. 40 (2009) 1290–1295.

[24] Y. Gao, N. Gao, H.D. Li, X.X. Yuan, Q.L. Wang, S.H. Cheng, J.S. Liu, Semiconductor SERS of diamond, Nanoscale 10 (2018) 15788–15792.

[25] W. Ji, L.F. Li, W. Song, X.N. Wang, B. Zhao, Y. Ozaki, Enhanced raman scattering by ZnO superstructures: synergistic effect of charge-transfer and mie resonance, Angew. Chem. Int. Ed. 58 (2019) 1–6.

[26] M. Faisal, A.A. Ismail, A.A. Ibrahim, H. Bouzid, S.A. Al-Sayari, Highly efficient photocatalyst based on ce doped ZnO Nanorods: controllable synthesis and enhanced photocatalytic activity, Chem. Eng. J. 229 (2013) 225–233.

[27] J.H. Yang, M. Gao, L.L. Yang, Y.J. Zhang, J.H. Lang, D.D. Wang, Y.X. Wang, H. L. Liu, H.G. Fan, M.B. Wei, F.Z. Liu, Synthesis and optical properties of Ce-Doped ZnO, Chem. Res. Chinese U. 24 (2008) 266–269.

[28] J.C. Yao, Y.N. Quan, M. Gao, R.X. Gao, L. Chen, Y. Liu, J.H. Lang, H. Shen, Y. Z. Zhang, L.L. Yang, J.H. Yang, AgNPs decorated Mg-Doped ZnO heterostructure with dramatic SERS activity for trace detection of food contaminants, J. Mater. Chem. C 7 (2019) 8199–8208.

[29] B. Chouchene, T.B. Chaabane, L. Balan, E. Girot, K. Mozet, G. Medjahdi, R. Schneider, High performance Ce-Doped ZnO nanorods for sunlight-driven photocatalysis, Beilstein J. Nanotechnol. 7 (2016) 1338–1349.

[30] Q. Luo, L.S. Wang, H.Z. Guo, K.Q. Lin, Y. Chen, G.H. Yue, D.L. Peng, Blue luminescence from ce-Doped ZnO thin films prepared by magnetron sputterin, Appl. Phys. A 108 (2012) 239–245.

[31] F. Li, B. Yan, J. Zhang, A.X. Jiang, C.H. Shao, X.J. Kong, X. Wang, Study on desulfmization efficiency and products of Ce-Doped nanosized ZnO desulfwizer at ambient tempemtm, J. Rare Earths 25 (2007) 306–310.

[32] M. Romeo, K. Bak, J. El Fallah, F. Le Normand, L. Hilaire, XPS Study of the reduction of cerium dioxide, Surf. Interface Anal. 20 (6) (1993) 508–512.

[33] M. Yousefifi, M. Amiri, R. Azimirad, A.Z. Moshfegh, Effect of annealing temperature on growth of Ce–ZnO nanocomposite thin films: X-ray photoelectron spectroscopy study, Thin Solid Films 520 (2011) 721–725.

[34] H. Borchert, Y.V. Frolova, V.V. Kaichev, I.P. Prosvirin, G.M. Alikina, A. I. Lukashevich, V.I. Zaikovskii, E.M. Moroz, S.N. Trukhan, V.P. Ivanov, E. A. Paukshtis, V.I. Bukhtiyarov, V.A. Sadykov, Electronic and chemical properties of nanostructured cerium dioxide doped with praseodymium, J. Phys. Chem. B 109 (2005) 5728–5738.

[35] Y.N. Quan, J.C. Yao, S. Yang, L. Chen, Y. Liu, J.H. Lang, H.Q. Zeng, J.H. Yang, M. Gao, Detect, remove and re-use: sensing and degradation pesticides via 3D Tilted ZMRs/Ag arrays, J. Hazard. Mater. 391 (2020) 122222–122228.

[36] J. Kubackova, G. Fabriciova, P. Miskovsky, D. Jancura, S. Sanchez-Cortes, Sensitive surface-enhanced raman spectroscopy (SERS) detection of organochlorine pesticides by alkyl dithiol-functionalized metal nanoparticles-Induced plasmonic hot spots, Anal. Chem. 87 (2015) 663–669.

[37] J.Y. Zhu, M.W. Jiang, H. Ma, H.J. Zhang, W.N. Cheng, J.B. Li, L.J. Cai, X.X. Han, B. Zhao, Redox-State-Mediated regulation of cytochrome c release in apoptosis revealed by surface-enhanced raman scattering on nickel substrates, Angew. Chem. Int. Ed. 58 (2019) 1–6.

[38] T.D. Vu, E. Jang, J. Lee, D. Choi, J. Chang, H. Chung, Feasibility of voltage-applied SERS measurement of bile juice as an effective analytical scheme to enhance discrimination between gall bladder (GB) polyp and GB Cancer, Anal. Chem. 92 (2020) 8159–8169.

[39] Y.Y. Zhu, Y.L. Cai, L.G. Xu, L.X. Zheng, L.M. Wang, B. Qi, C.L. Xu, Building an aptamer/graphene oxide FRET biosensor for one-step detection of bisphenol A, ACS Appl. Mater. Interfaces 7 (2015) 7492–7496.

[40] Y.N. Quan, J.C. Yao, S. Yang, L. Chen, J. Li, Y. Liu, J.H. Lang, H. Shen, Y.X. Wang, Y.Y. Wang, J.H. Yang, M. Gao, ZnO Nanoparticles on MoS_2 Microflowers for ultrasensitive SERS detection of bisphenol A, Microchim. Acta 186 (2019) 593–600.

[41] X.M. Han, C.S.L. Koh, H.K. Lee, W.S. Chew, X.Y. Ling, Microchemical plant in a liquid droplet: Plasmonic liquid marble for sequential reactions and attomole detection of toxin at Microliter-Scale, ACS Appl. Mater. Interfaces 9 (2017) 39635–39640.

[42] Q.Q. Zhang, X.S. Li, Q. Ma, Q. Zhang, H. Bai, W.C. Yi, J.Y. Liu, J. Han, G.C. Xi, A metallic molybdenum dioxide with high stability for surface enhanced raman spectroscopy, Nat. Commun. 8 (2017) 14903–14911.

[43] L. Qiu, Q. Liu, X.L. Zeng, Q. Liu, X.D. Hou, Y.F. Tian, L. Wu, Sensitive detection of bisphenol A by coupling solid phase microextraction based on monolayer graphene-coated Ag nanoparticles on si fibers to surface enhanced raman spectroscopy, Talanta 187 (2018) 13–18.

[44] P.Y. Lin, C.W. Hsieh, S. Hsieh, Rapid and sensitive SERS detection of bisphenol a using self-assembled graphitic substrates, Sci. Rep. 7 (2017) 16698–16704.

[45] Y.B. Xie, Y.J. Meng, SERS performance of graphene oxide decorated silver nanoparticle/Titania nanotube array, RSC Adv. 4 (2014) 41734–41743.